

RESEARCH

Open Access



Enhanced photocatalytic removal of nitric oxide over Ag-decorated ZnSn(OH)₆ microcubes

Minh-Thuan Pham^{1,2,3}, Nguyen Thi Van², Truc Mai Thi Nguyen⁴, Hong-Huy Tran⁵, Hieu Trung Nguyen^{1,3}, Jheng-Jie Jiang², Sheng-Jie You^{2,3} and Ya-Fen Wang^{2,3*} 

Abstract

Presently, most of the population has been facing a string of severe air pollution problems that include the intensive emission of nitric oxide (NO), which requires a practical approach to sustain our living conditions. Herein, Ag nanoparticles (Ag NPs)-decorated ZnSn(OH)₆ microcubes (Ag:cZHS) photocatalysts are synthesized and used for photocatalytic NO removal under solar light activation. The properties of the newly obtained photocatalysts are comprehensively characterized by a series of typical methods. The NO removal performance over the cZHS photocatalysts was increased markedly upon being combined with Ag NPs because of the surface plasmon resonance effect. The contribution of electron (e⁻), hole (h⁺), hydroxyl radical (•OH), and oxygen radicals (•O₂) was investigated through trapping tests and electron spin resonance analysis. Also, the by-products and apparent quantum efficiency of the photocatalysts were thoroughly studied.

Keywords: ZnSn(OH)₆, Surface plasmon resonance, Photocatalysis, Silver, Nitric oxide

1 Introduction

In recent decades, with the rapid development of advanced industries, environmental pollution has become increasingly severe [1, 2]. The mass emission of several toxic gases such as carbon dioxide, methane, and nitrogen oxide (NO_x) from manufacturing, transportation, factory, and power plant activities represents an pressing concern to the global environment and human health [3]. Arguably, the NO_x is one of the leading greenhouse gases directly causing global warming [4, 5].

Nitric oxide (NO) is a primary component of NO_x released during combustion processes [6], the NO removal from the atmosphere is an important task for solving air pollution problems. Extensive research on photocatalytic NO removal from ambient air has been performed using various methods, such as selective catalytic reduction,

selective non-catalytic reduction, biofiltration, adsorption, absorption, and photocatalytic technology [7–10]. Among them, photocatalytic technology has attracted much attention due to its great potential for pollutant degradation efficiency, low-cost, non-toxic, and eco-friendly [11, 12]. Recently, a wide range of photocatalysts has been studied for NO gas removals, such as bismuth (III) oxide [13], zinc hydroxystannate microcubics (cZHS) [14], graphitic carbon nitride [15], tin oxide [16] and titanium dioxide [17]. Among these materials, cZHS presents a highly promising photocatalyst, especially in addressing air pollution. However, its wide bandgap (~3.7 eV) remains the key challenge for the widespread use of cZHS under visible light irradiation [14].

Therefore, several methods have been implemented to reduce the bandgap of cZHS materials, including the combination with noble metals (gold, copper, silver), metal oxides (zinc oxide, tin oxide) [11, 18, 19], and non-metals (carbon, sulfur) [20, 21]. The metal decoration is one of the best ways to enhance the photocatalytic performance of the materials thank to the surface plasmon

* Correspondence: yfwang@cycu.edu.tw

²Department of Environmental Engineering, Chung Yuan Christian University, Taoyuan 32023, Taiwan

³Center for Environmental Risk Management, Chung Yuan Christian University, Taoyuan 32023, Taiwan

Full list of author information is available at the end of the article



© The Author(s). 2022 **Open Access** This article is licensed under a Creative Commons Attribution 4.0 International License, which permits use, sharing, adaptation, distribution and reproduction in any medium or format, as long as you give appropriate credit to the original author(s) and the source, provide a link to the Creative Commons licence, and indicate if changes were made. The images or other third party material in this article are included in the article's Creative Commons licence, unless indicated otherwise in a credit line to the material. If material is not included in the article's Creative Commons licence and your intended use is not permitted by statutory regulation or exceeds the permitted use, you will need to obtain permission directly from the copyright holder. To view a copy of this licence, visit <http://creativecommons.org/licenses/by/4.0/>.

resonance (SPR) effect [22, 23]. Herein, silver nanoparticles (Ag NPs) are well-known as a good combination with other semiconductors due to their excellent chemical and conductivity properties [24], which can reduce their bandgap and thereby improve photocatalytic efficiency. The SPR effect from Ag NPs enhances the lifetime of electron and hole pairs by accelerating the transfer of electrons on the surface of the materials. In addition, Ag is the most suitable metal due to its ease of preparation, well-studied, and reasonable cost.

In this work, Ag NPs are decorated on the surface of cZHS materials to enhance the photocatalytic performance through the SPR effect. Specially, cZHS materials are prepared by the hydrothermal method, and the silver nitrate (AgNO_3) is reduced by pluronic[®]127 (F127) to form Ag NPs at the high temperature ($\geq 100^\circ\text{C}$) [25, 26]. The photocatalytic NO removal is monitored by an analyzer that met the USEPA requirements for the RFNA-1289-074 method, and the international standard-ISO 22197-1. The photocatalytic mechanism of Ag:cZHS materials is determined experimentally by the photodegradation of NO under solar light. In addition, the characterizations of materials are studied by various techniques. Significantly, the presence of SPR of Ag NPs is identified by diffuse reflectance spectroscopy (DRS). The results of this work promise to provide a new and effective way to address NO pollution.

2 Experiments

2.1 Preparation of $\text{ZnSn}(\text{OH})_6$ microcubes

The F127 solution was prepared by adding 1.4 g of F127 (CAS: 9003-11-6, Sigma-Aldrich) into 300 mL of deionized water and 200 mL of 98% ethanol. The synthesis process of

cZHS is illustrated in Fig. 1. In this work, 7.5 mL of 2 mM zinc acetate dihydrate (98%, $\text{C}_4\text{H}_{10}\text{O}_6\text{Zn}$, CAS: 5970-45-6, ACROS Organics) and 7.5 mL of 2 mM tin (IV) chloride pentahydrate ($\text{SnCl}_4 \cdot 5\text{H}_2\text{O}$, CAS: 10026-06-9, Sigma-Aldrich) were mixed and stirred for 30 min until the solution becomes transparent. Next, 15 mL of 0.28 wt% F127 and 6 mL of 3 M sodium hydroxide solution were added into the mixture and stirred for 30 min to achieve a homogeneous solution, and a white precipitate was formed during this step. Finally, this solution was transferred into a 50 mL Teflon-lined stainless steel autoclave for the hydrothermal step at 100°C for 10 h. The samples were rinsed with deionized water and ethanol until the pH reaches the value of about 6.0, followed by a drying step at 80°C to obtain cZHS.

2.2 Preparation of Ag nanoparticles-decorated $\text{ZnSn}(\text{OH})_6$ microcubes

The preparation of Ag:cZHS is shown in Fig. 1. A Teflon-lined autoclave for the hydrothermal process was fastly cooled down by tap water. Then, the different amounts of 0.1 M AgNO_3 (CAS: 7761-88-8, Sigma-Aldrich) were added into the hot cZHS and stirred in 30 min. The solution turned to light-gray color after the addition of AgNO_3 . Then, the solutions were rinsed with ethanol and deionized water several times and dried at 80°C to produce Ag:cZHS with 5, 10, 15, 20 and 30 wt% of the expected Ag denoted as 5% Ag:cZHS, 10% Ag:cZHS, 20% Ag:cZHS and 30% Ag:cZHS, respectively.

2.3 The photocatalytic experiments

For the photocatalytic test, 0.2 g of the catalysts was dispersed into a petri dish ($d = 14\text{ cm}$) by 10 mL of deionized water and treated by ultrasonicator for 3 min,

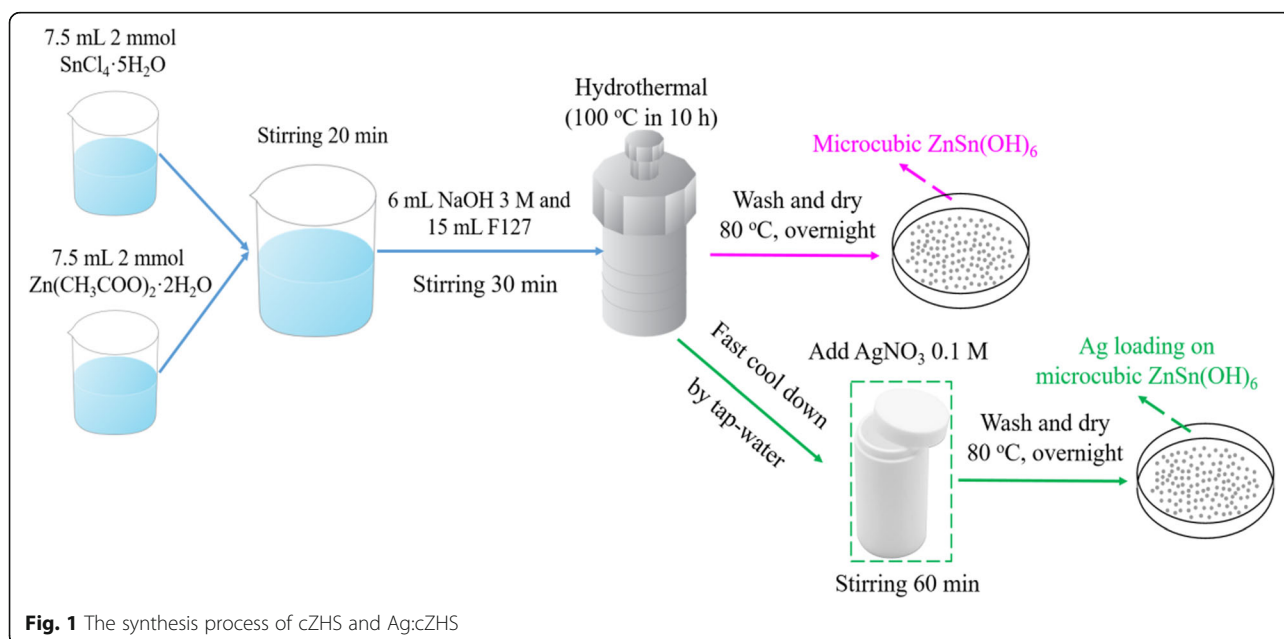


Fig. 1 The synthesis process of cZHS and Ag:cZHS

followed by a drying step at 80 °C for 30 min to eliminate water. Then, the catalyst was placed in a photocatalytic reactor tank (volume = 3 L). The reactor tank is made of stainless steel with a quartz-sealed top to allow light to penetrate the surface of the photocatalyst.

The NO analyzer met the USEPA requirements for RFNA-1289-074. First, the NO 100 ppm (N₂ balanced, Ming Yang Co.) was diluted with zero air to reach a concentration of 500 ppb for the experimental process. The gas input was controlled by mass flow controllers; the pressure value of NO source and zero air source was 240 kPa and 310 kPa, respectively. The relative humidity and flow rate adjusted at 50% and 1.5 L min⁻¹, respectively. The concentrations of NO, and nitrogen dioxide (NO₂) was recorded with a NO_x analyzer (model 42c, Thermo-Science). To eliminate the adsorption capacity of the material, the fabric and NO gas interact with each other in the dark environment for about 10 to 15 min until the concentration of the gases reached equilibrium. Then, a 300 W xenon lamp (950 nm > λ > 200 nm) was turned on for 15 min., as the solar power source of this experiment. The full spectra of the xenon lamp are shown in Fig. S1 of Supplemental Materials.

The recycling test attested to the durability of the catalyst. Here, the catalyst was washed with water and dried after completion of each photocatalytic experiment, and repeated five times. The trapping test determined the critical factors of NO photocatalytic degradation. The potassium iodide (KI), isopropyl alcohol (IPA), and dichromate solution (K₂Cr₂O₇) scavengers were added to trap h⁺, •OH, and e⁻ [13, 27]. The NO degradation, NO₂ conversion, apparent quantum efficiency (AQE), and the kinetic reaction rate were evaluated by Eqs. (S1), (S2), (S3), and (S4), respectively [28, 29].

2.4 Characterizations

Fourier transform infrared spectrophotometer (FTIR) analysis was established in the range of 400–4000 cm⁻¹ by using Jasco FT/IR-6500 to investigate molecular vibrations. X-ray diffraction (XRD) patterns were used to determine the materials' phase composition and crystal structure. This analysis was carried out using Bunaciu, Udristioiu, and Aboul-Enein 2015 X-ray diffractometer with the Cu K radiation (λ = 0.154 nm) and the scanning rate of 6° min⁻¹ in the 2θ range of 10–80°. The surface and crystal morphology of the materials was observed by scanning electron microscopy (SEM) and transmission electron microscopy (TEM). The SEM images were captured using Hitachi FE-SEM S-4800 N, and the TEM image was developed by the JEOL JEM 2000FXI model; samples were dispersed in ethanol and coated on a copper mesh for analysis. The high-resolution TEM (HR-TEM) was invested to determine the d-spacing of Ag NPs. X-ray photoelectron spectroscopy (XPS) analysis

was also conducted for more investigation about the surface elemental composition and elemental states. Furthermore, the materials' optical property and surface area were examined using diffuse reflectance spectroscopy (DRS) analysis and Brunauer-Emmett-Teller (BET) analyzer, respectively. The electron spin resonance (ESR) was invested to determine the generation of oxygen radicals (•O₂) and •OH.

3 Results and discussion

3.1 Photocatalytic activity

The photocatalytic NO removal efficiencies of the cZHS and Ag:cZHS materials under solar light are shown in Fig. 2a. The photocatalytic NO removal efficiencies of the blank, cZHS, 1% Ag:cZHS, 5% Ag:cZHS, 10% Ag:cZHS, 20% Ag:cZHS, and 30% Ag:cZHS materials are 13, 54, 52, 62, 68, 87, and 81%, respectively. The photocatalytic NO removal efficiency significantly increased upon being combined with Ag NPs, likely indicating the effect of the SPR of Ag NPs. In detail, the photocatalytic NO removal efficiency of the cZHS increases 8, 14, 33, and 27% with the 5, 10, 20, and 30% of Ag NPs decorated on the cZHS, respectively. However, the photocatalytic NO removal efficiency of the 1% Ag:cZHS decreases by about 2% compared to the cZHS. These results indicate that the photocatalytic activity of the materials can be decreased by adding too little or too much Ag NPs. Besides, the kinetic reaction rate constants are calculated by the Langmuir-Hinshelwood function (Fig. S2). The reaction rate's constants of the cZHS, 1% Ag:cZHS, 5% Ag:cZHS, 10% Ag:cZHS, 20% Ag:cZHS, 30% Ag:cZHS are 0.14, 0.091, 0.13, 0.19, 0.32, and 0.25 min⁻¹, respectively. In addition, the photocatalytic NO removal efficiency of the 20% Ag:cZHS reaches 88% after only 7 min and remains unchanged. In contrast, the photocatalytic NO removal efficiency of the cZHS increases slowly during the reaction and reaches the highest NO removal efficiency of 60% after 15 min. Thus, the 20% Ag:cZHS is the most efficient sample. Practically speaking, the reusability of materials is important, which is evaluated by a series of recycling tests. As shown in Fig. 2b, after the light is turned on, the NO concentration in the reaction decreases sharply and remained plateau for 15 min of the reaction until the light is turned off. The photocatalytic NO removal efficiencies of the 20% Ag:cZHS are 87, 85, 80, 79, and 78% at the first, second, third, fourth, and fifth cycle, respectively. The result shows that the photocatalytic NO removal efficiency of the 20% Ag:cZHS decreases from 87 to 78% after 4 times recycling at the same condition, an insignificant loss of NO removal efficiency after several times of reaction could be owing to the accumulation of degradation product generated from photocatalytic reactions [30]. The results indicate that the durability of the sample is promising,

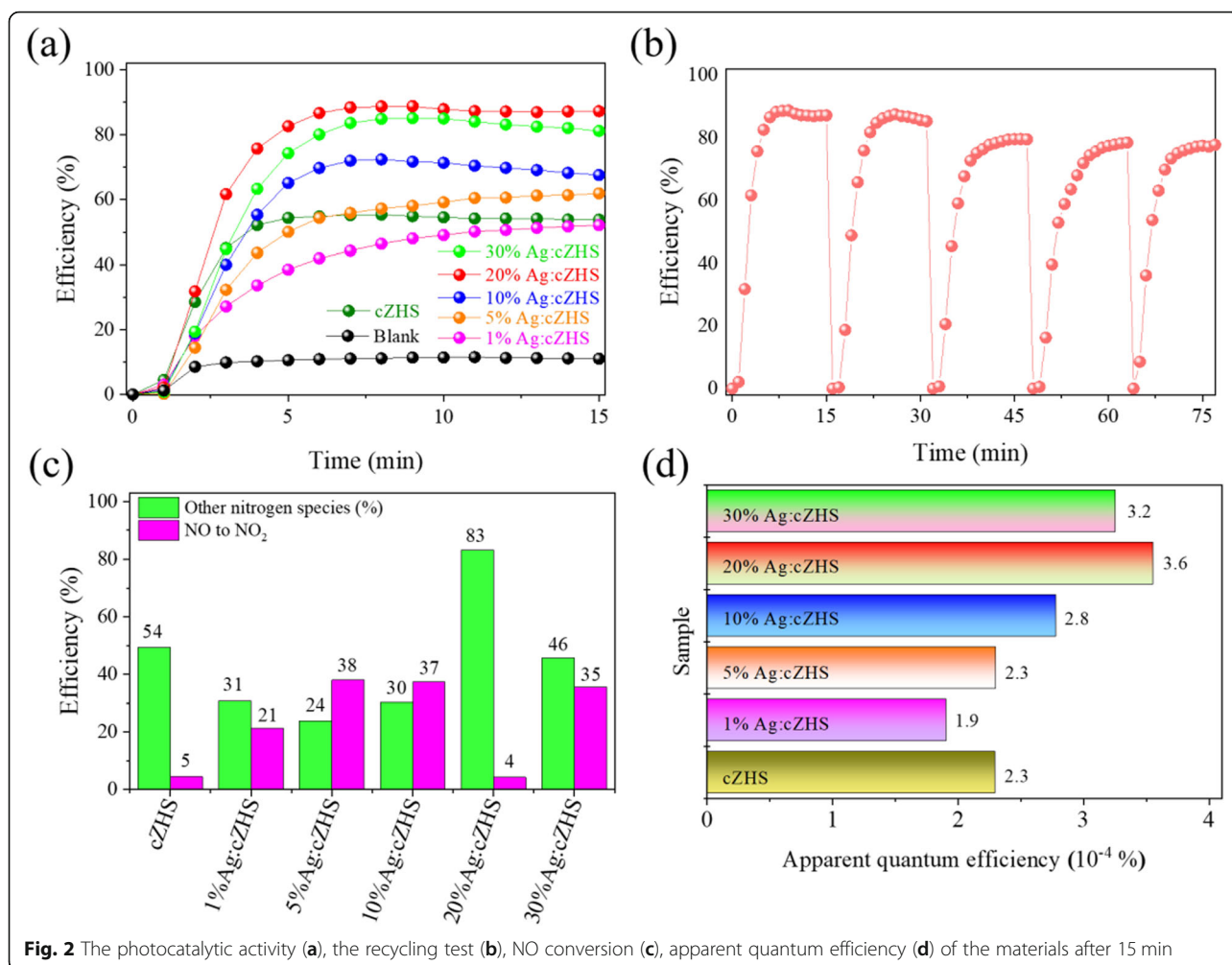


Fig. 2 The photocatalytic activity (a), the recycling test (b), NO conversion (c), apparent quantum efficiency (d) of the materials after 15 min

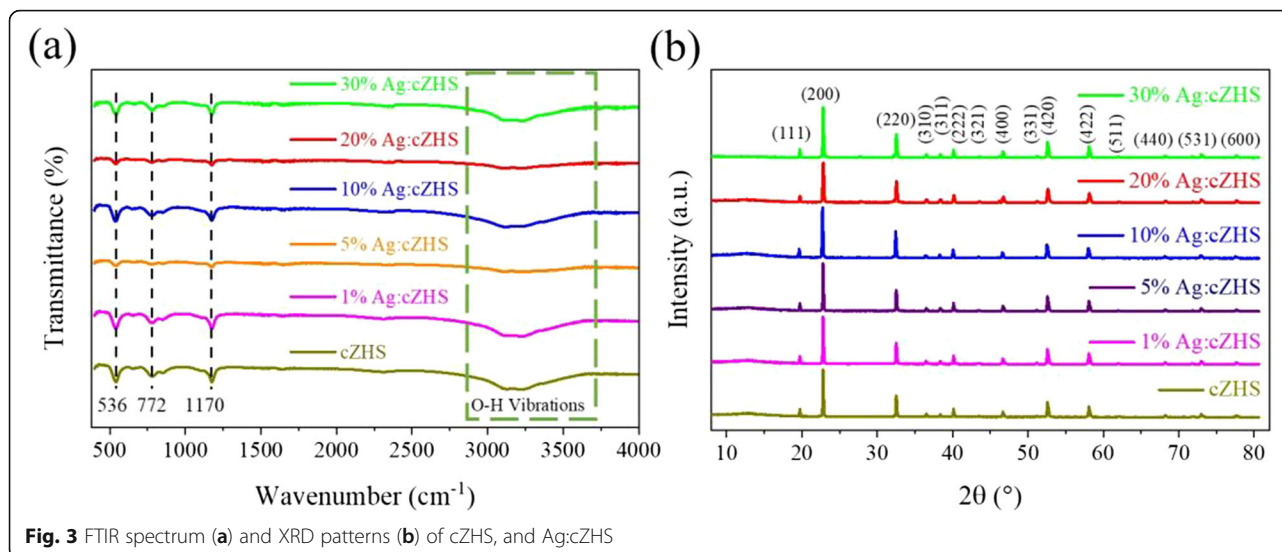
and its photostability is sufficient for long-term usage in reality. The NO₂ selectivity is shown in Fig. S3, the concentrations of NO₂ generated by the cZHS, 1% Ag:cZHS, 5% Ag:cZHS, 10% Ag:cZHS, 20% Ag:cZHS, 30% Ag:cZHS materials is 23, 109, 141, 189, 22, and 182 ppb, respectively. Based on the NO₂ selectivity (Fig. S3), the conversion of NO to NO₂ and other nitrogen species is also calculated as shown in Fig. 2c. In Fig. 2c, the 20% Ag:cZHS showed the lowest NO₂ generation (4%), and the highest other nitrogen species generation (83%). The NO₂ generation efficiencies of the cZHS, 1% Ag:cZHS, 5% Ag:cZHS, 10% Ag:cZHS, 20% Ag:cZHS, 30% Ag:cZHS is 5, 21, 38, 37, and 35%, respectively. Since the main components of NO_x are NO and NO₂, the low generation of NO₂ demonstrates that the material has a good photocatalytic ability to remove NO and NO₂. The other nitrogen species (N₂O, NO₂⁻, NO₃⁻, etc.) generation efficiencies of the cZHS, 1% Ag:cZHS, 5% Ag:cZHS, 10% Ag:cZHS, 30% Ag:cZHS are 54, 31, 24, 30, and 46%, respectively. The AQE is calculated by Eq. (S3) to understand the effect of photons on the photocatalytic ability of the Ag:

cZHS and cZHS (Fig. 2d). The AQE (10⁻⁴%) values of the cZHS, 1% Ag:cZHS, 5% Ag:cZHS, 10% Ag:cZHS, 20% Ag:cZHS, 30% Ag:cZHS are 2, 2, 3, 4, and 3, respectively.

3.2 Material characterizations

Figure 3a shows the FTIR spectra of the 1% Ag:cZHS, 5% Ag:cZHS, 10% Ag:cZHS, 20% Ag:cZHS, 30% Ag:cZHS and cZHS, in the range from 400 to 4000 cm⁻¹. The wide peak observed in 3800 to 2750 cm⁻¹ shows OH bending and stretching vibrations [11]. Besides, the sharp peak appears at 1170 cm⁻¹, attributes to Sn–OH deformation vibration [31]. The stretching vibration of Sn–O–Sn is observed at 779 and 536 cm⁻¹ [32]. The results obtained confirm the success of the cZHS synthesis, but the signal of Zn and Ag are difficult to detect by the FTIR analysis. Therefore, the XRD diffraction is carried out to confirm the structure and crystallization of cZHS.

The XRD patterns of all samples are shown in Fig. 3b. The results show that several characteristic peaks locate at 19.7, 22.8, 32.7, 36.43, 38.5, 40.3, 45.9, 52.8, 58.3, 62.5,



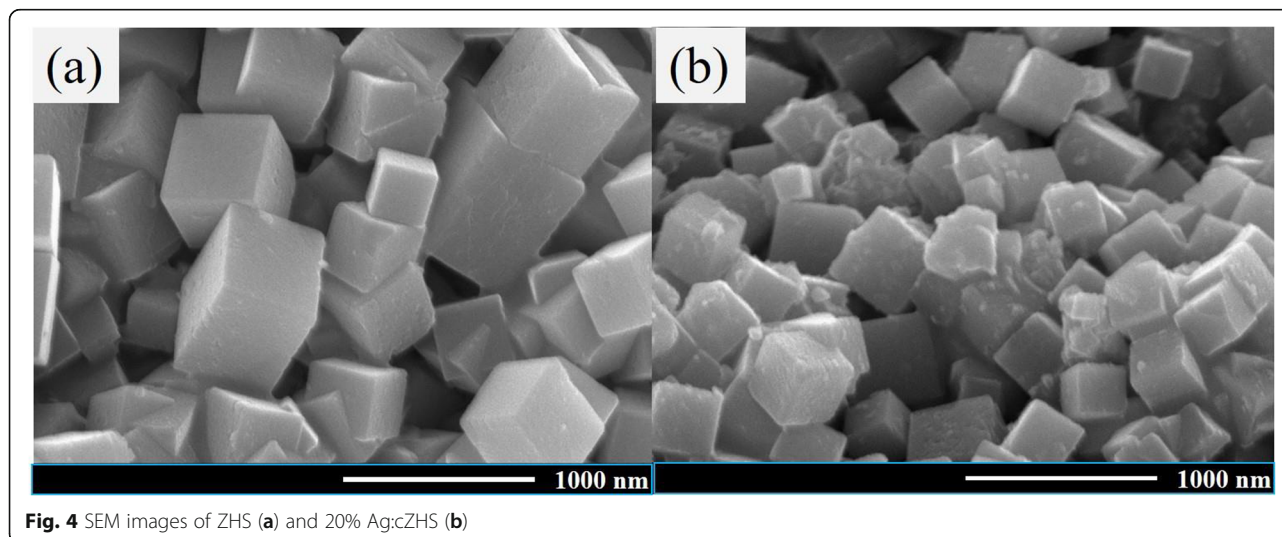
68.0, 73.0, and 77.0° corresponding to the (111), (200), (220), (310), (311), (222), (400), (420), (422), (511), (440), (531), and (600) lattice planes of the cZHS, respectively (from JCPDS 74–1825). The results indicate that the cZHS has been successfully synthesized and has crystallinity with high purification in the cube phase. Furthermore, small additional peaks overlapped at 38.0, 45.0, 64.5, and 77.4° could be attributed to the (111), (200), (220), and (311) planes of the Ag NPs in the Ag:cZHS samples, respectively [33]. However, the peaks that appeared on the XRD pattern could not prove the presence of Ag NPs in the Ag:cZHS samples due to peak overlap. Thus, the HR-TEM is also performed to clarify the issue.

3.3 Morphology of materials

The SEM images in Fig. 4 shows the cube shape of the sample before and after Ag NPs loading. As show in Fig.

4a, the cZHS is synthesized with precise cube shapes with smooth surfaces. The cZHS is dispersed well in the solvent, without any conglomeration. It could be seen in Fig. 4b that the original morphology of the cZHS is changed when Ag NPs are loaded onto the surface. The shape and structure of the Ag:cZHS become distinctive. However, the change is not much, which proves that this synthesis method do not change the morphology of the substrate material. The SEM demonstrates that the Ag NPs successfully loaded onto the cZHS surface. The EDS mapping and the wt% of the materials are shown in Fig. S4 and Table S1.

Figure 5 shows the morphology and structure of the cZHS and 20% Ag:cZHS. As shown in Fig. 5a and b, the TEM images of the pristine cZHS show precise edges, and the length ranging from 300 to 600 nm matches well with SEM images. It is observed in Fig. 5c and d that the presence of Ag NPs is



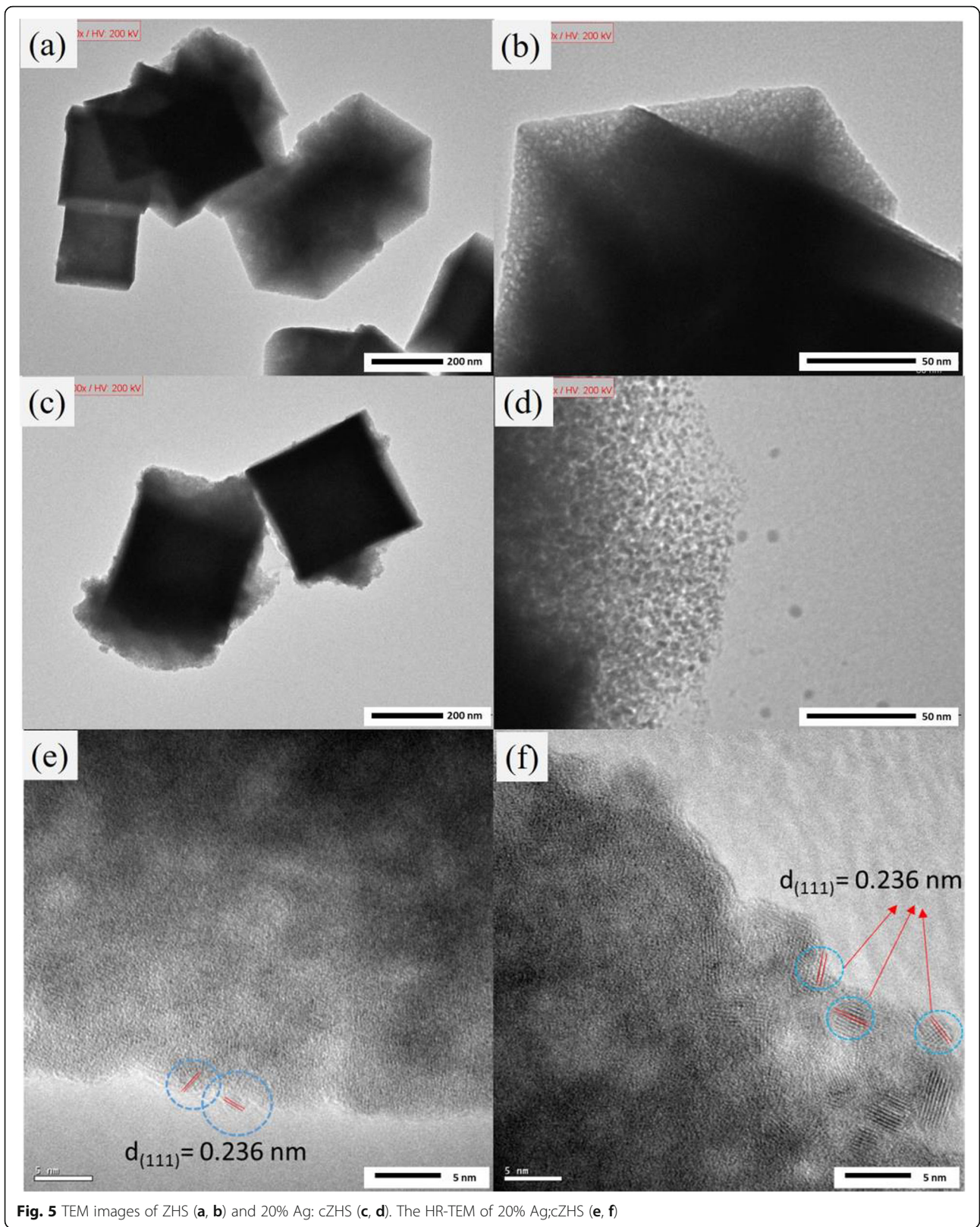


Fig. 5 TEM images of ZHS (a, b) and 20% Ag: cZHS (c, d). The HR-TEM of 20% Ag:cZHS (e, f)

covered on the surface of the cZHS cubes with a diameter less than 10 nm. Furthermore, the dots that appear in Fig. 5d are predicted to be Ag NPs. In contrast, in Fig. 5b, the dots of Ag NPs do not appear; instead, the nanopores are created by the F127. These nanopores are filled with Ag NPs in the 20% Ag cZHS. As show in Fig. 5e and f, the d-spacing of Ag NPs is 0.236 nm, corresponding to the (111) plane of Ag NPs. The HR-TEM results confirm that F127 reduced the AgNO_3 at 100 °C to form Ag NPs [34].

3.4 The specific surface area of the materials

The N_2 adsorption isotherms of the cZHS and 20% Ag:cZHS are shown in Fig. 6. The adsorbed quantity of the cZHS is higher than that of the 20% Ag:cZHS. In addition, the BET surface areas of the cZHS and 20% Ag:cZHS are 20 and 35 $\text{m}^2 \text{g}^{-1}$, respectively. The total pore volume and average pore width of the cZHS and the 20% Ag:cZHS are 0.034 $\text{cm}^3 \text{g}^{-1}$, 6.70 nm, and 0.027 $\text{cm}^3 \text{g}^{-1}$, 3.97 nm, respectively. These results confirm that the higher total pore volume and average pore width of the cZHS are due to the presence of F127, which increase the porosity of the sample [35]. The hypothesis that the Ag NPs filled the nanopores of the cZHS has been determined by the lower total pore volume and average pore width of the 20% Ag:cZHS. The higher specific surface area of the 20% Ag:cZHS may be explained by the small pore size diameter (3.61 nm) and the nano size of the Ag NPs. The smaller particles have a higher specific surface area [36]. Herein, the Ag NPs with the nanosize affect the particular surface area of the

material. These points can be understood as decreasing the particle size employed an increase in the specific surface area. The high specific surface area also confirms that Ag NPs are well dispersed on the surface of the materials [37].

3.5 Optical properties of materials

The optical absorption properties of the cZHS and 20% Ag:cZHS are shown in Fig. 7. In Fig. 7a, the 20% Ag:cZHS could reflect photons with a wavelength in the range of UV light ($400 \text{ nm} > \lambda > 200 \text{ nm}$). The wavelength of about 260 and 360 nm are the peaks of SPR, which are generated by Ag NPs. Besides, the formation of a peak of SPR in the range of UV ($240 \text{ nm} < \lambda < 260 \text{ nm}$) and the DRS tail of the 20% Ag:cZHS do not coincide with the Ox axis in the range of IR. In contrast, in the cZHS, there is a peak present at around 360 nm. The morphology of this peak is bizarre and attributed to the manipulation of the DRS operator. However, after repeated measurements of DRS, we conclude that the appearance of this peak of the cZHS sample is due to the influence of F127 on the surface of the material. At the wavelength of about 350 to 380 nm, there is a superposition between the two peaks, so the peak of F127 may have been masked by the SPR peak of Ag NPs. The previous studies also determined the superposition of the peak at 360 nm of F127. The peak at 360 nm could be covered by any peaks that have more vigorous intensity than this at the same wavelength [38, 39]. As show in Fig. 7b, Kubelka-Munk plots of DRS reveal that the band

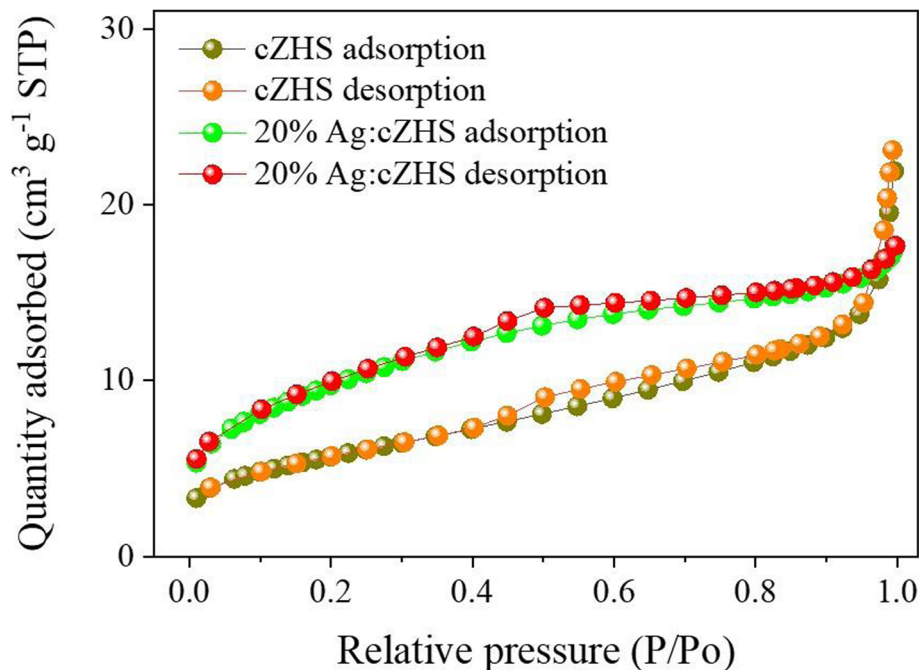
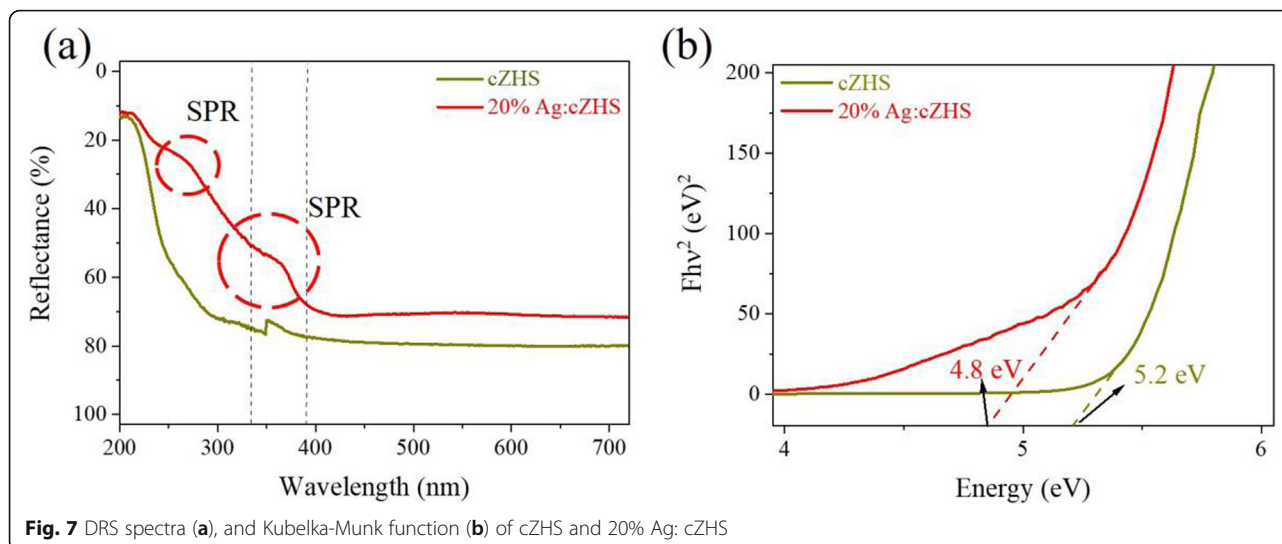


Fig. 6 N_2 adsorption-desorption isotherms of cZHS and 20% Ag:cZHS



structure of cZHS is an indirect transition with the bandgap of 5.2 eV. The 20% Ag:cZHS has a smaller bandgap (4.8 eV), which is expected to have better photocatalytic activity.

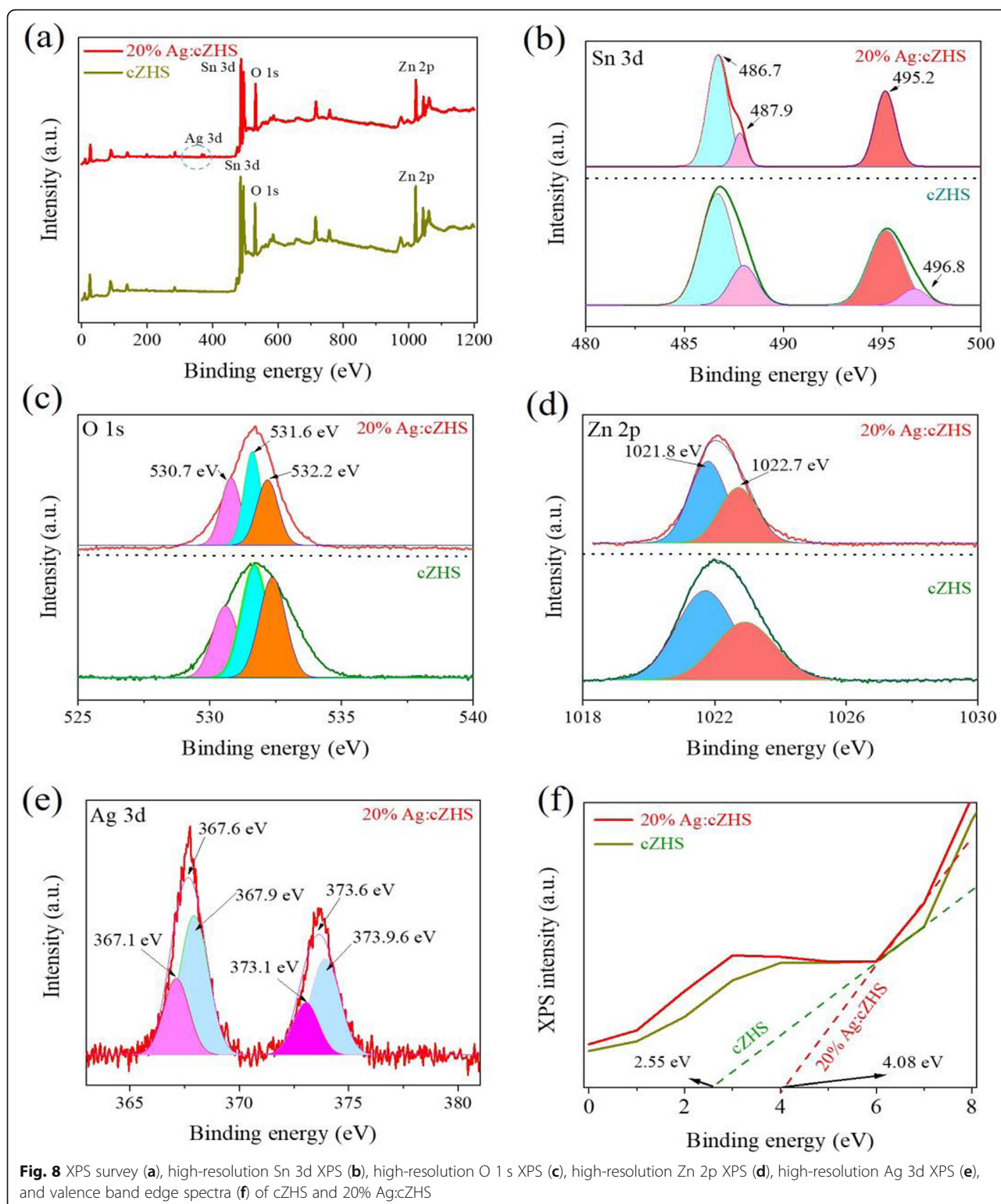
The surface chemistry of materials is shown in Fig. 8. Figure 8a shows that the peaks of Sn 3d, O 1s, and Zn 2p of cZHS. Furthermore, the peak around 370 eV of the 20% Ag:cZHS corresponds to the Ag 3d. The HR-XPS of Sn 3d_{5/2}, O 1s, and Zn 2p_{3/2} are shown in Fig. 8b, c, and d, respectively. The peaks at 485.3 eV, 493.8 eV correspond to Sn 3d_{5/2}, Sn 3d_{3/2} for Sn⁴⁺ state in the cZHS, respectively [40]. The peak at 531 eV, 1022 eV correspond to O 1s, and Zn 2p_{3/2}, respectively. As show in Fig. 8c, the peak at 531.6 eV is assigned to the metal-oxygen bonds (Sn-O or Zn-O), the peak at 530.7, and 532 eV are assigned to the metal-hydroxyl bonds (Zn-OH or Sn-OH) and hydroxyl absorbed on the surface of the materials [41]. In Fig. 8d, the peak at 1021.8 eV is assigned to the Zn-hydroxyl (Zn-OH) bonding of the cZHS [42]. The HR-XPS of Ag 3d is shown in Fig. 8e; two peaks of Ag 3d at 367.6 and 373.6 eV, corresponding to Ag 3d_{5/2} and Ag 3d_{3/2} for Ag²⁺ in the 20% Ag:cZHS, respectively. The peaks at 367.9 eV and 373.6 eV are assigned to the Ag⁺ in silver-oxygen interaction (Ag-O) and metallic Ag [43]. In addition, XPS is a directly used tool to measure the valence-band maximum (VBM) of the materials. As show in Fig. 8f, the VBM of the cZHS is 2.55 eV, and 20% Ag:cZHS is 4.08, the VBM of 20% Ag:cZHS is 1.53 eV higher than the cZHS, it is revealed that the electrons provided by Ag lead to the enhancement of electron transport in the composites.

3.6 Photocatalytic mechanism over the materials

The trapping test considers the critical factors of photocatalytic degradation of NO, as show in Fig. 9. In the trapping test (Fig. 9a), the h⁺, e⁻, and •OH are trapped

by adding the KI, K₂Cr₂O₇, and IPA scavengers, respectively. The photocatalytic NO removal efficiencies of the 20% Ag:cZHS are 62, 57, and 37% after 15 min with the trapping of •OH, h⁺, e⁻, respectively. The trapping results indicate that e⁻ and •OH almost have the same influence on the photocatalytic activity of 20% Ag:cZHS. The photocatalytic efficiency of the 20% Ag:cZHS is decreased dramatically (37%) by adding KI. The ESR is invested in determining the generation of radicals of 20% Ag:cZHS. Figure 9b and Fig. S5 shows that the 20% Ag:cZHS generate more •OH than •O₂. However, the intensity of •O₂ and •OH are also strong. These results explain that in the 20% Ag:cZHS, the •OH is formed by h⁺, and the e⁻ react with O₂ to form •O₂ at the same time.

Based on the experimental evidence and previous studies [11, 14, 44], the proposed mechanism on the photocatalytic NO removal of the Ag:cZHS under solar light is presented in Fig. 10. Under light activation, the e⁻ - h⁺ pairs are generated in the cZHS. The photo-generated e⁻ spontaneously move to the conduction band of the cZHS and is isolated by the interface between the cZHS and the Ag NPs [45]. These e⁻ reduce the adsorbed O₂ on the surface to produce •O₂, as evidenced from the ESR results. The photo-generated e⁻ in the Ag NPs and cZHS is transported between the Ag NPs and cZHS to increase the lifetime of the e⁻ - h⁺ pairs. The photo-generated h⁺ in the valence band of the cZHS oxidize the adsorbed water on the surface of the cZHS to form •OH radicals. The •O₂ and •OH radicals assist in the removal of NO [46]. Thus, the introduction of the Ag NPs drastically enhance photocatalytic NO removal by the cZHS through the surface plasmonic effect, resulting in a better photoresponse and excellent electron-hole pairs separation. Besides, the NO degradation pathway is also shown in Fig. 10. Firstly, the •O₂



and $\bullet\text{OH}$ are reacted with NO to form NO_2 . Then, NO_2 reacts with water to form nitrate (NO_3^-) and nitric (NO_2^-) in the forms of nitric acid (HNO_3) and nitrous acid (HNO_2), respectively. HNO_2 and HNO_3 are a cause

of acid rain. On the other hand, the HNO_2 also reacts with $\bullet\text{OH}$ to form NO_2 . Then, NO_2 reacts with $\bullet\text{OH}$ to form NO_3^- and hydron (H^+). The formation of by-products (exclude NO_2), such as N_2O , N_2 , N_2O_5 , etc.,

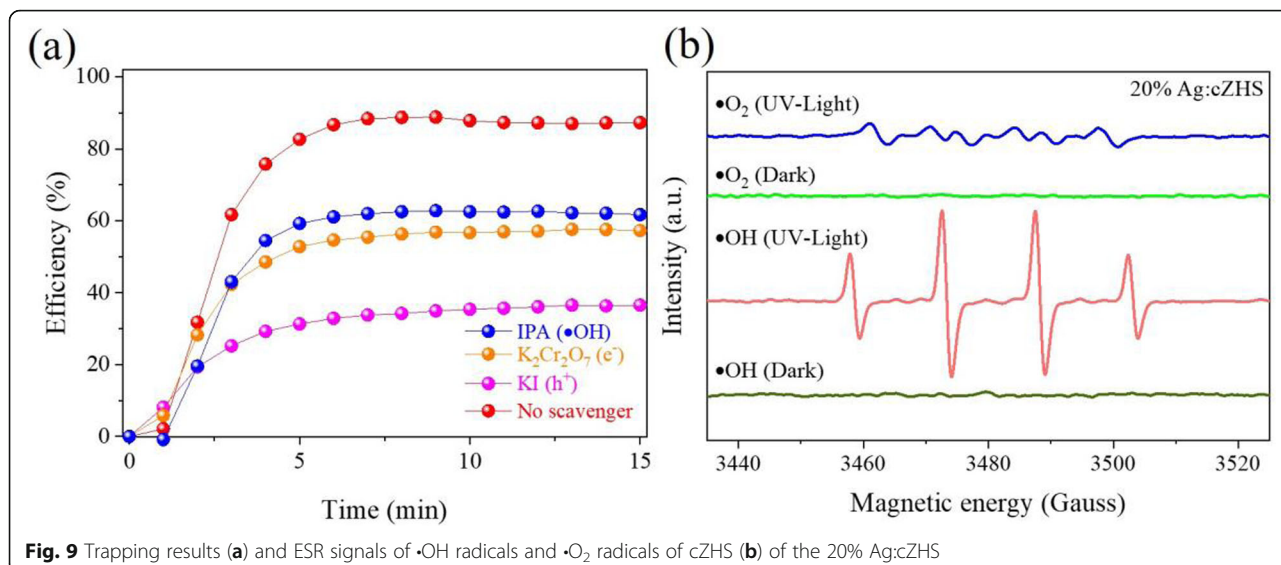


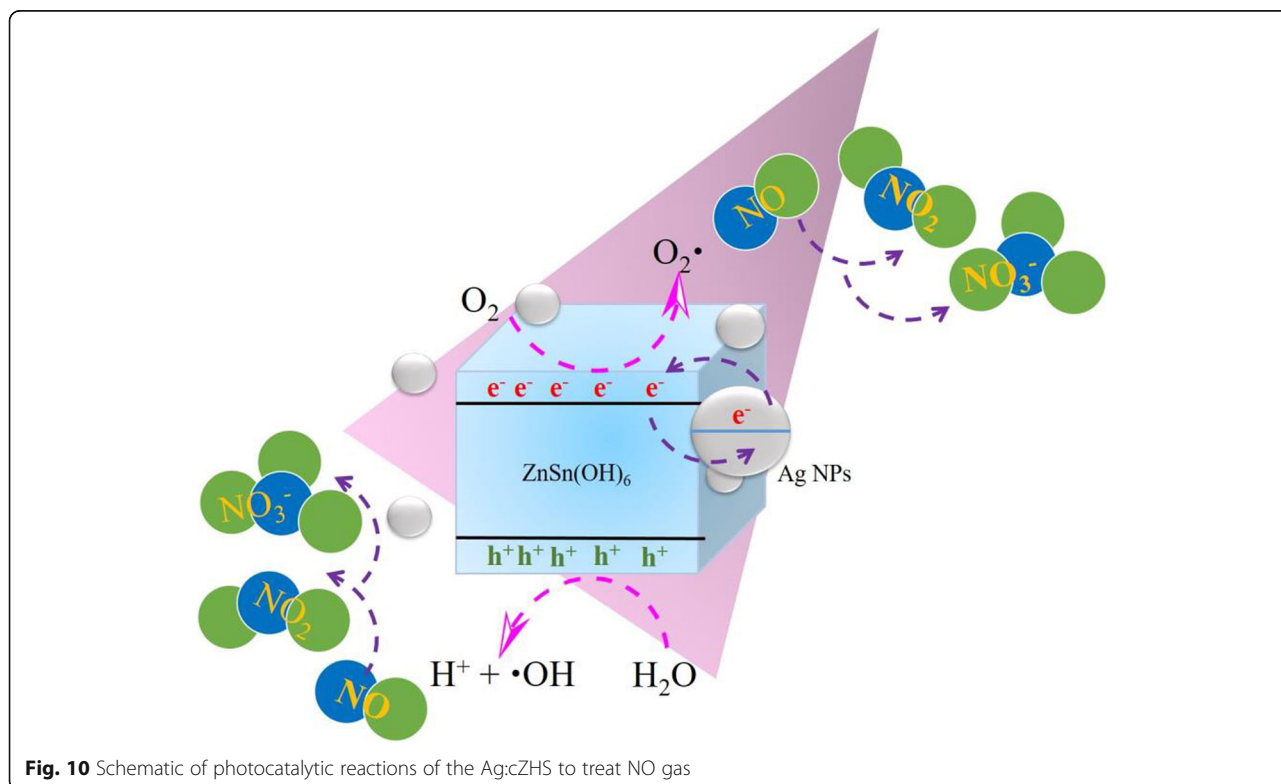
Fig. 9 Trapping results (a) and ESR signals of •OH radicals and •O₂ radicals of cZHS (b) of the 20% Ag:cZHS

from NO and NO₂, is also predicted by other studies [47–49]. However, the selectivity of those gas is not recorded because of the limitation of the equipment.

4 Conclusions

In this work, the Ag:cZHS nanocomposite photocatalysts were prepared by a rapid and straightforward physical mixing process. The as-prepared Ag:cZHS nanocomposite photocatalysts showed a remarkable improvement of

NO removal under solar light through the surface plasmonic effect from Ag NPs. With 20% of Ag loading, a photocatalytic performance of 87% was achieved, much higher than that of the bare cZHS (52%). This sample also had a good photostability and recycling ability with a photocatalytic performance of approximately 77% even after five repetitive runs. Besides, the effect of SPR on photocatalytic activity was confirmed by DRS. The peak of SPR appeared at the wavelength of about 360 nm and



260 nm. The trapping results and ESR determined that the h^+ and $\bullet OH$ were the main factors in the photocatalytic activity of the 20% Ag:cZHS. This study presents the promise of Ag:cZHS nanocomposite photocatalysts for addressing air pollution.

5 Supplementary Information

The online version contains supplementary material available at <https://doi.org/10.1186/s42834-022-00125-y>.

Additional file 1. Supplementary materials.

Acknowledgments

We want to present our gratitude to Chung Yuan Christian University, Taoyuan City, Taiwan; Center for Environmental Risk Management, Chung Yuan Christian University, Taoyuan City, Taiwan; Department of Civil Engineering Chung Yuan Christian University, Taoyuan City, Taiwan; Department of Environmental Engineering, Chung Yuan Christian University, Taoyuan City, Taiwan; Center for Environmental Toxin and Emerging-Contaminant Research, Cheng Shiu University, Kaohsiung, Taiwan, ROC; Université Grenoble Alpes, CNRS, Grenoble INP (Institute of Engineering, Université Grenoble Alpes), LMGP, 38000 Grenoble, France.

Authors' contributions

Minh-Thuan Pham: methodology (recycle test, trapping test), visualization, writing-original draft, editing, data curation. Van-Thi Nguyen: methodology (photocatalytic test, synthesis materials). Truc-Mai Thi Nguyen: data curation, investigation, editing. Hong-Huy Tran: data curation, investigation, editing. Hieu Trung Nguyen: editing. Jheng-Jie Jiang: investigation, visualization. Sheng-Jie You: formal analysis (FTIR, XRD, SEM, NO analysis), project administration. Ya-Fen Wang: formal analysis (XPS, ESR, NO analysis, TEM), chemical conceptualization, supervision, funding acquisition. All authors read and approved the final manuscript.

Funding

This work is supported by the Chung Yuan Christian University with project number 109609432.

Availability of data and materials

All data generated or analyzed during this study are included in this published article (and its [supplementary information files](#)).

Declarations

Competing interests

We declare there are no competing financial interests.

Author details

¹Department of Civil Engineering, Chung Yuan Christian University, Taoyuan 32023, Taiwan. ²Department of Environmental Engineering, Chung Yuan Christian University, Taoyuan 32023, Taiwan. ³Center for Environmental Risk Management, Chung Yuan Christian University, Taoyuan 32023, Taiwan. ⁴Center for Environmental Toxin and Emerging-Contaminant Research, Cheng Shiu University, Kaohsiung 83347, Taiwan. ⁵French National Center for Scientific Research, University of Grenoble Alpes, 38000 Grenoble, France.

Received: 19 August 2021 Accepted: 27 January 2022

Published online: 22 February 2022

References

- Chao YC, Hsieh TC, Chen CW, Cheng CT, Li HC, Yeh KC, et al. Impact assessment of reservoir desiltation measures for downstream riverbed migration in climate change: a case study in northern Taiwan. *J Hydro-Environ Res.* 2021;37:67–81.
- Marazziti D, Cianconi P, Mucci F, Foresi L, Chiarantini I, Della Vecchia A. Climate change, environment pollution, COVID-19 pandemic and mental health. *Sci Total Environ.* 2021;773:145182.
- Saini J, Dutta M, Marques G. A comprehensive review on indoor air quality monitoring systems for enhanced public health. *Sustain Environ Res.* 2020;30:6.
- Bungadaeng S, Prueksasit T, Siriwong W. Inhalation exposure to respirable particulate matter among workers in relation to their e-waste open burning activities in Buriram Province, Thailand. *Sustain Environ Res.* 2019;29:26.
- Erme K, Jogi I. Metal oxides as catalysts and adsorbents in ozone oxidation of NO_x. *Environ Sci Technol* 2019;53:5266–71.
- Li XH, Chen XM, Hu GX, Li LX, Su HN, Wang YY, et al. Response to the Svingen comments on Li et al. effects of in utero exposure to dicyclohexyl phthalate on rat fetal Leydig cells. *Int J Environ Res Public Health.* 2016;13:533.
- Gao L, Mi XH, Zhou Y, Li W. A pilot study on the regeneration of ferrous chelate complex in NO_x scrubber solution by a biofilm electrode reactor. *Bioresour Technol.* 2011;102:2605–9.
- Hu JD, Chen DY, Li NJ, Xu QF, Li H, He JH, et al. In situ fabrication of Bi₂O₃/CO₃/MoS₂ on carbon nanofibers for efficient photocatalytic removal of NO under visible-light irradiation. *Appl Catal B-Environ.* 2017;217:224–31.
- Boubnov A, Carvalho HWP, Doronkin DE, Gunter T, Gallo E, Atkins AJ, et al. Selective catalytic reduction of NO over Fe-ZSM-5: mechanistic insights by operando HERFD-XANES and valence-to-core X-ray emission spectroscopy. *J Am Chem Soc.* 2014;136:13006–15.
- Meditana SR, Tirukkovalluri SR, Raju IM, Alim SA, Jaishree G, Chippada MLVP. Gemini surfactant assisted synthesis of mesoporous Mn/Mg bimetal doped TiO₂ nanomaterial: characterization and photocatalytic activity studies under visible light irradiation. *Sustain Environ Res.* 2021;31:6.
- Pham MT, Bui DP, Lin F, Phuong NH, Huang Y, Cao JJ, et al. Enhanced near-visible-light photocatalytic removal of formaldehyde over Au-assisted ZnSn(OH)₆ microcubes. *Environ Technol Inno.* 2020;20:101112.
- Li X, Yu JG, Jaroniec M. Hierarchical photocatalysts. *Chem Soc Rev.* 2016;45:2603–36.
- Pham MT, Hussain A, Bui DP, Nguyen TMT, You SJ, Wang YF. Surface plasmon resonance enhanced photocatalysis of Ag nanoparticles-decorated Bi₂S₃ nanorods for NO degradation. *Environ Technol Innov.* 2021;23:101755.
- Pham MT, Tran HH, Nguyen TMT, Bui DP, Huang Y, Cao JJ, et al. Revealing DeNO_x and DeVOC reactions via the study of the surface and bandstructure of ZnSn(OH)₆ photocatalysts. *Acta Mater.* 2021;215:117068.
- Li X, Dong GH, Guo FJ, Zhu PF, Huang Y, Wang CY. Enhancement of photocatalytic NO removal activity of g-C₃N₄ by modification with illite particles. *Environ Sci-Nano.* 2020;7:1990–8.
- Huy TH, Phat BD, Thi CM, Viet PV. High photocatalytic removal of NO gas over SnO₂ nanoparticles under solar light. *Environ Chem Lett.* 2019;17:527–31.
- Duan YY, Zhang M, Wang L, Wang F, Yang LP, Li XY, et al. Plasmonic Ag-TiO_{2-x} nanocomposites for the photocatalytic removal of NO under visible light with high selectivity: the role of oxygen vacancies. *Appl Catal B-Environ.* 2017;204:67–77.
- Lu YF, Huang Y, Cao JJ, Li HW, Ho WK, Lee SC. Constructing Z-scheme SnO₂/N-doped carbon quantum dots/ZnSn(OH)₆ nano hybrids with high redox ability for NO_x removal under VIS-NIR light. *J Mater Chem A.* 2019;7:15782–93.
- Yu XJ, Lu HX, Li Q, Zhao YL, Zhang LW, Fan BB, et al. Hydrothermal synthesis and characterization of micro/nanostructured ZnSn(OH)₆/ZnO composite architectures. *Cryst Res Technol.* 2011;46:1175-80.
- Zhang YY, Wang LL, Yang ML, Wang J, Shi JS. Carbon quantum dots sensitized ZnSn(OH)₆ for visible light-driven photocatalytic water purification. *Appl Surf Sci.* 2019;466:515–24.
- Lian XY, Chen Z, Yu X, Fan TT, Dong YY, Zhai HS, et al. Enhancing the photocatalytic activity of ZnSn(OH)₆ achieved by gradual sulfur doping tactics. *Nanoscale.* 2019;11:9444–56.
- Hou WB, Cronin SB. A review of surface plasmon resonance-enhanced photocatalysis. *Adv Funct Mater.* 2013;23:1612–9.
- Menon S, Agarwal H, Shanmugam VK. Catalytic degradation of industrial dyes using biosynthesized selenium nanoparticles and evaluating its antimicrobial activities. *Sustain Environ Res.* 2021;31:2.
- Gangadharan P, Nambi IM. The performance of Cu²⁺ as dissolved cathodic electron-shuttle mediator for Cr⁶⁺ reduction in the microbial fuel cell. *Sustain Environ Res.* 2020;30:19.
- Iqbal M, Chung YI, Tae G. An enhanced synthesis of gold nanorods by the addition of Pluronic (F-127) via a seed mediated growth process. *J Mater Chem.* 2007;17:335–42.
- Wu C, Xia GM, Sun J, Song R. Synthesis and anisotropic self-assembly of Ag nanoparticles immobilized by the Pluronic F127 triblock copolymer for colorimetric detection of H₂O₂. *RSC Adv.* 2015;5:97648–57.

27. Xu X, Sun YF, Fan ZH, Zhao DQ, Xiong SM, Zhang BY, et al. Mechanisms for O^{2-} and $\cdot OH$ production on flowerlike $BiVO_4$ photocatalysis based on electron spin resonance. *Front Chem*. 2018;6:64.
28. Ohtani B. Photocatalysis by inorganic solid materials: revisiting its definition, concepts, and experimental procedures. *Adv Inorg Chem*. 2011;63:395–430.
29. Vasanth Kumar K, Porkodi K, Rocha F. Langmuir-Hinshelwood kinetics – a theoretical study. *Catal Commun*. 2008;9:82–4.
30. Liu Y, Yu S, Zhao ZY, Dong F, Dong XA, Zhou Y. N-doped $Bi_2O_2CO_3$ /graphene quantum dot composite photocatalyst: enhanced visible-light photocatalytic NO oxidation and in situ DRIFTS studies. *J Phys Chem C*. 2017;121:12168–77.
31. Odeh AO. Qualitative and quantitative ATR-FTIR analysis and its application to coal char of different ranks. *J Fuel Chem Technol*. 2015;43:129–37.
32. Wan WJ, Li YH, Ren XP, Zhao YP, Gao F, Zhao HY. 2D SnO_2 nanosheets: synthesis, characterization, structures, and excellent sensing performance to ethylene glycol. *Nanomaterials-Basel*. 2018;8:112.
33. Ahmad MB, Shamel K, Darroudi M, Yunus WMZW, Ibrahim NA. Synthesis and characterization of silver/clay nanocomposites by chemical reduction method. *Am J Appl Sci*. 2009;6:1909–14.
34. Zhao XY, Zhang J, Wang BS, Zada A, Humayun M. Biochemical synthesis of Ag/AgCl nanoparticles for visible-light-driven photocatalytic removal of colored dyes. *Materials*. 2015;8:2043–53.
35. Samsudin EM, Abd Hamid SB, Juan JC, Basirun WJ. Influence of triblock copolymer (pluronic F127) on enhancing the physico-chemical properties and photocatalytic response of mesoporous TiO_2 . *Appl Surf Sci*. 2015;355:959–68.
36. Liu YT, Zhang QP, Xu M, Yuan H, Chen Y, Zhang JX, et al. Novel and efficient synthesis of Ag-ZnO nanoparticles for the sunlight-induced photocatalytic degradation. *Appl Surf Sci*. 2019;476:632–40.
37. Zhang QP, Xu XN, Liu YT, Xu M, Deng SH, Chen Y, et al. A feasible strategy to balance the crystallinity and specific surface area of metal oxide nanocrystals. *Sci Rep*. 2017;7:46424.
38. Mohamed MM, Khairy M, Eid S. Surfactant-assisted formation of silver titanates as active catalysts for methanol electro-oxidation. *Appl Catal A*. 2017;547:205–13.
39. Zhou H, Zhong ST, Shen M, Yao YF. Composite soft template-assisted construction of a flower-like $\beta-Bi_2O_3/Bi_2O_2CO_3$ heterojunction photocatalyst for the enhanced simulated sunlight photocatalytic degradation of tetracycline. *Ceram Int*. 2019;45:15036–47.
40. Li HQ, Hong WS, Cui YM, Jia QF, Fan SH. High photocatalytic activity of $C-ZnSn(OH)_6$ catalysts prepared by hydrothermal method. *J Mol Catal A*. 2013;378:164–73.
41. Wang H, Yuan XZ, Wu Y, Zeng GM, Tu WG, Sheng C, et al. Plasmonic Bi nanoparticles and BiOCl sheets as cocatalyst deposited on perovskite-type $ZnSn(OH)_6$ microparticle with facet-oriented polyhedron for improved visible-light-driven photocatalysis. *Appl Catal B-Environ*. 2017;209:543–53.
42. Chen F, Yang Q, Niu CG, Li XM, Zhang C, Zhao JW, et al. Enhanced visible light photocatalytic activity and mechanism of $ZnSn(OH)_6$ nanocubes modified with AgI nanoparticles. *Catal Commun*. 2016;73:1–6.
43. Zhang C, He DH, Fu SS, Zeng GM, Liang QH, Yang Y, et al. Silver iodide decorated $ZnSn(OH)_6$ hollow cube: room-temperature preparation and application for highly efficient photocatalytic oxytetracycline degradation. *Chem Eng J*. 2021;421:129810.
44. Viet PV, Nguyen HP, Tran HH, Bui DP, Hai LV, Pham MT, et al. Constructing $g-C_3N_4/SnO_2$ S-scheme heterojunctions for efficient photocatalytic NO removal and low NO_2 generation. *J Sci-Adv Mater Dev*. 2021;6:551–9.
45. Bui DP, Nguyen MT, Tran HH, You SJ, Wang YF, Viet PV. Green synthesis of $Ag@SnO_2$ nanocomposites for enhancing photocatalysis of nitrogen monoxide removal under solar light irradiation. *Catal Commun*. 2020;136:105902.
46. Huy TH, Phat BD, Kang F, Wang YF, Liu SH, Thi CM, et al. SnO_2/TiO_2 nanotube heterojunction: the first investigation of NO degradation by visible light-driven photocatalysis. *Chemosphere*. 2019;215:323–32.
47. Roy S, Madras G. Photocatalytic NOx abatement: a short review. *Curr Org Chem*. 2015;19:2122–31.
48. Angelo J, Andrade L, Madeira LM, Mendes A. An overview of photocatalysis phenomena applied to NOx abatement. *J Environ Manag*. 2013;129:522–39.
49. Luevano-Hipolite E, Martinez-de la Cruz A. Enhanced photocatalytic activity of TiO_2 rutile by coupling with fly ashes for the removal of NO gases. *Ind Eng Chem Res*. 2016;55:11512–9.

Publisher's Note

Springer Nature remains neutral with regard to jurisdictional claims in published maps and institutional affiliations.

Ready to submit your research? Choose BMC and benefit from:

- fast, convenient online submission
- thorough peer review by experienced researchers in your field
- rapid publication on acceptance
- support for research data, including large and complex data types
- gold Open Access which fosters wider collaboration and increased citations
- maximum visibility for your research: over 100M website views per year

At BMC, research is always in progress.

Learn more [biomedcentral.com/submissions](https://www.biomedcentral.com/submissions)

